



저작자표시-비영리-변경금지 2.0 대한민국

이용자는 아래의 조건을 따르는 경우에 한하여 자유롭게

- 이 저작물을 복제, 배포, 전송, 전시, 공연 및 방송할 수 있습니다.

다음과 같은 조건을 따라야 합니다:



저작자표시. 귀하는 원저작자를 표시하여야 합니다.



비영리. 귀하는 이 저작물을 영리 목적으로 이용할 수 없습니다.



변경금지. 귀하는 이 저작물을 개작, 변형 또는 가공할 수 없습니다.

- 귀하는, 이 저작물의 재이용이나 배포의 경우, 이 저작물에 적용된 이용허락조건을 명확하게 나타내어야 합니다.
- 저작권자로부터 별도의 허가를 받으면 이러한 조건들은 적용되지 않습니다.

저작권법에 따른 이용자의 권리는 위의 내용에 의하여 영향을 받지 않습니다.

이것은 [이용허락규약\(Legal Code\)](#)을 이해하기 쉽게 요약한 것입니다.

[Disclaimer](#)

이학석사 학위논문

Dark-field and SERS  
spectroscopic study on  
nanoparticle-molecule-thin film  
junction

나노입자-분자-금 박막에 대한  
암시야 및 표면증강라만산란 연구

2018년 8월

서울대학교 대학원  
화학부 물리화학전공

이승연

M. S. Dissertation

Dark-field and SERS  
spectroscopic study on  
nanoparticle-molecule-thin film  
junction

Supervisor : Professor Zee Hwan Kim

August 2018

By Seung Yeon Lee

Department of Chemistry

The Graduate School

Seoul National University

# Abstract

The localized surface plasmon resonance (LSPR) was largely investigated because it is the key factor of nanoparticle (NP) application. However, the role of molecules and quantum mechanical phenomenon such as tunneling effect was underrated in LSPR investigation. In this research, we observed the tunneling effect on LSPR by the dark-field spectroscopy. We used two systems to reduce the heterogeneity of LSPR originated from the metal structure: changing molecules in the junction by photoreduction and using well-defined single-crystalline junction. First, photoreduction of 4-nitrobenzenethiol (NBT) was used to change the molecules in the Ag nanoparticle (AgNP)-NBT-Au thin film (AuTF) junction. This allowed us to obtain the scattering spectrum of one junction with different molecules. Second, we synthesized atomically flat single-crystalline micron-size Au platelet to substitute the AuTF. The NPs were also substituted with well-defined nanocubes (NC) which have atomically flat single-crystalline surface. This allowed us to obtain the scattering spectrum with less heterogeneity and observe the tunneling effect on LSPR.

To obtain the scattering signal, we constructed a home-built confocal dark-field spectroscopy set-up. The collection efficiency was largely improved compared to the common dark-field spectroscopy or the reported confocal dark-field spectroscopy by removing the scattering signal from nearby junctions and collecting the signal in a high-NA region where the scattering signal radiates a lot. Also, using the correlated surface-enhanced Raman

spectroscopy (SERS) set-up by the beam splitter, we can obtain the SERS spectrum of the targeted junction simultaneously.

Using photoreduction of NBT to 4-aminobenzenethiol (ABT), we can change the molecules in one junction without changing the metal structure. The blue-shift of LSPR was observed in most of the junctions. Because all other factors such as welding of nanoparticles, a difference of refractive index, or charging effect are negligible in this system, blue-shift of LSPR is originated from the tunneling coefficient change. Although the additional experiment is needed to observe exact LSPR shift distribution, this result shows the possibility of adjusting LSPR of metal nanostructure simply by changing the adsorbed molecules.

With the modified version of micron-size Au platelet synthesis reported previously, we synthesized wide (side length  $> 5 \mu\text{m}$ ) and thin (thickness :  $\sim 30 \text{ nm}$ ) Au platelet. The surfactant was removed by solvent wash. The additional experiment with different molecules is needed to investigate the tunneling effect on LSPR in this system.

**Keyword : LSPR, Dark-field spectroscopy, tunneling effect, photoreduction, single-crystal**

**Student Number : 2016-20355**

# Table of Contents

Abstract .....	i
Table of Figures .....	iv
<b>Chapter 1. Introduction .....</b>	<b>1</b>
1.1. Localized surface plasmon resonance.....	1
1.2. The LSPR of the NP–molecule–AuTF.....	6
<b>Chapter 2. Experimental Set–up .....</b>	<b>12</b>
<b>Chapter 3. Investigation of tunneling effect on LSPR : photoreduction of NBT .....</b>	<b>15</b>
3.1. The photoreduction of NBT.....	15
3.2. The LSPR shift during NBT reduction.....	18
<b>Chapter 4. Investigation of tunneling effect on LSPR : single–crystalline junction.....</b>	<b>25</b>
4.1. Synthesis of Au platelet .....	25
4.2. Fabrication of single–crystalline junction .....	27
<b>Conclusion.....</b>	<b>32</b>
<b>Bibliography .....</b>	<b>33</b>
<b>Abstract (in Korean) .....</b>	<b>37</b>

## Table of Figures

**Figure 1** The two perspectives of LSPR investigation.<sup>1</sup> The schematic diagram of (a) classical electromagnetic perspective and (b) quantum mechanical perspective. The spectrum of (c) classical electromagnetic perspective calculation and (d) quantum mechanical perspective calculation shows the opposite trend as the gap distance decreases. In quantum mechanical perspective, the calculation was done by setting an imaginary dielectric medium in the gap which can represent the tunneling effect properties. Figures are modified from the ref 1 with permission. Copyright © 2012, Springer Nature..... 2

**Figure 2** (a) The previous calculation<sup>12</sup> and (b) experiment<sup>13</sup> research which showed the tunneling effect on LSPR. The  $G_0$  in (a) represents unit conductance and large conductance means high tunneling coefficient. Figures are modified from the ref 12, 13 with permission. Copyright © 2010 American Chemical Society, Copyright © 2014 American Chemical Society. .... 5

**Figure 3** LSPR spectrum (calculation) of the AgNP–molecule–AuTF junctions with (a) different gap distance (refractive index of molecule layer : 1.4, AuTF thickness : 30 nm) and (b) different refractive index of molecule layer (gap distance : 1.4 nm, AuTF thickness : 10 nm). The calculation was done by finite–difference time–domain (FDTD) method. The CRC model (Au), Palik model (Ag), and 1.4 (molecule layer) were used for the refractive index of each layer and diameter of AgNP is 80 nm. (c) The reported LSPR spectrum (experiment)<sup>18</sup> which showed the effect of nanoparticle size on LSPR in the AgNP–molecule–AuTF junctions. (d) The reported LSPR

spectrum (calculation)<sup>15</sup> which showed the effect of the contact area of nanoparticles. Figure (c) and (d) are modified from the ref 18, 15 with permission. Copyright © 2016 American Chemical Society, Copyright © 2017 American Chemical Society. .... 7

**Figure 4** The schematic diagram of the (a) AgNP–molecule–AuTF junctions and the (b) AgNC–molecule–Au platelet junctions used in this experiment. The black inset shows the structure of the molecules we introduced in each junction. 4–nitrobenzenethiol (NBT) and 4–aminobenzenethiol (ABT) were introduced in the AgNP–molecule–AuTF junctions, and 4–methylbenzenethiol (MBT) and mercaptobenzoic acid (MBA) were introduced in the AgNC–molecule–Au platelet junctions. (c) The calculated scattering spectrum of the AgNP–molecule–AuTF junctions shows one strong LSPR from dipole mode near 600 nm and (d) the calculated scattering spectrum of the AgNC–molecule–Au platelet shows one strong LSPR from dipole mode near 1200 nm and two weak LSPRs from higher order modes in the visible region. The insets show the electric field distribution of each LSPR on the top of the molecule layer (xy–plane, scalebar : 20 nm). The calculation was done by FDTD and the CRC model (Au), Palik model (Ag), and 1.4 (molecule layer) were used for the refractive index of each layer. The thickness of AuTF (10 nm) and Au platelet (30 nm), size of AgNP (diameter : 80 nm) and AgNC (side length : 80 nm), and gap distance (1.9 nm) were determined by the real value of each structure. .... 8

**Figure 5** The schematic diagram (a, b, c) and a cross–section of the output signal (d, e, f) of the (a, d) general dark field set–up, (b, e) the reported confocal dark–field set–up<sup>18</sup>, and (c, f) the home–built confocal dark–field set–up. The blue line represents the incident

beam, the light-blue line represents the reflection beam, and the light-red line represents the scattering signal from the sample.... 11

**Figure 6** The schematic diagram of the home-built confocal dark-field/SERS set-up. The blue line represents the incident beam of the supercontinuum laser for the dark-field spectroscopy and the red line represents the incident beam of the HeNe laser for the SERS spectroscopy. Two incident light sources were correlated with 5 : 5 broadband beam splitter. The light-blue line represents the reflection beam of the supercontinuum laser and the light-red line represents the scattering signal from the sample. The sphere-like beam block was used to block the reflection beam of supercontinuum laser in front of the Raman spectrometer. This was substituted into the Raman notch filter to block the strong Rayleigh scattering when we obtained the SERS spectrum..... 14

**Figure 7** (a) The schematic diagram of NBT photoreduction and (b) the SERS spectrum of each molecule<sup>2</sup>. (c) The real-time SERS spectrum obtained in the AgNP-NBT-AuTF junctions shows that we can track the reaction with the intensity of *vs* (*NO*). The graph on the right side of (c) implies that most (> 90 %) of NBT is reduced to ABT rather than DMAB.<sup>2</sup> Figure (b) and (c) are modified from the ref 2. Copyright © 2016 American Chemical Society..... 17

**Figure 8** (a) The schematic diagram of the change in the AgNP-NBT-AuTF junctions and (b) the scattering spectrum of the junction. .... 18

**Figure 9** (a) The scattering spectrum of the AgNP-NBT-AuTF junctions before (red) and after (blue) the HeNe laser irradiation in one junction. (c) The SERS spectrum obtained during the HeNe laser irradiation (start : red, end : blue) in the same junction. (c) The

schematic diagram of the molecular change in the AgNP–NBT–AuTF junction during the HeNe laser irradiation. (d) The histogram of  $\Delta\lambda_{LSPR}$  in 10 junctions. The LSPR shift was calculated by the equation  $\Delta\lambda_{LSPR} = \lambda_{ABT} - \lambda_{NBT}$ . The peak position was obtained by measuring the maximum position of the smoothed spectrum. The smoothing was done by Gaussian-type smoothing with  $\sigma = 15$ . The average peak shift and standard deviation obtained by Gaussian fitting is 7.2 nm blue-shift and 7.0 nm. .... 19

**Figure 10** (a) The real-time scattering spectrum during the supercontinuum laser irradiation. Each spectrum was smoothed with the Gaussian-type smoothing ( $\sigma = 20$ ). The black line shows the maximum point of the smoothed spectrum. (b) The scattering spectrum profile shows a temporal shift in one junction. The spectrum below (red) shows the scattering spectrum profile at the time pointed with a red arrow in (a) and the spectrum above (blue) shows the scattering spectrum profile at the time pointed with a blue arrow in (a). The colored arrow in b shows the maximum point of each spectrum. (c) The SERS spectrum after the supercontinuum laser irradiation shows that the negligible number of NBT is reduced. The black arrows indicate the three main SERS peaks of NBT. .... 21

**Figure 11** (a) The scattering spectrum of the AgNP–MBT–AuTF junction. The power of the HeNe laser and irradiation time was maintained similar to the AgNP–NBT–AuTF junction experiment. (b) The histogram of  $\Delta\lambda_{LSPR}$  in 7 junctions. The determination of peak position and  $\Delta\lambda_{LSPR}$  is same as the method presented in Figure 9. .... 22

**Figure 12** (a) The calculated LSPR spectrum<sup>19</sup> with the different contact area. The laser irradiation can weld the AgNP and shift LSPR

toward longer wavelength. (b) The calculated LSPR spectrum of the AgNP–molecule–AuTF junction with reported refractive index (NBT : 1.62, ABT : 1.665). Figure (a) is modified from the ref 19 with permission. Copyright 2015 by the American Physical Society.

..... 24

**Figure 13** (a) The schematic diagram of reported atomically flat single–crystalline micro–size Au platelet synthesis.<sup>25</sup> The (b) SEM image and the (c) XRD pattern shows the formation of single–crystalline Au platelet. Figure (b) and (c) are modified from the ref 25 with permission. Copyright © 2006 Elsevier B. V..... 26

**Figure 14** (a) The AFM topography of synthesized atomically flat single–crystalline micron–size Au platelet (scale bar : 2  $\mu\text{m}$ ) and the magnified AFM topography of Au platelet surface (inset, scale bar : 200 nm). (b) The AFM topography of constructed the AuNC–BPT–Au platelet junction (scale bar : 4  $\mu\text{m}$ ) and the magnified AFM topography of the junction in the red box (inset, scale bar : 200 nm). (c) The SERS spectrum of junction showed that surfactant of Au platelet and AuNC effectively removed by wash process. The black arrows indicate the three main SERS peaks of BPT. .... 29

# Chapter 1. Introduction

## 1.1. Localized surface plasmon resonance

The interaction between metal and light generates collective electron oscillation along the metal surface called surface plasmon. Especially, in metal nanoparticles (NPs), localized surface plasmon (LSP) which does not propagate and only exists near the NPs is generated. Near the certain wavelength called localized surface plasmon resonance (LSPR), large LSP is generated and the scattering or the absorbance increases. Therefore, by observing the scattering spectrum or the absorption spectrum, we can investigate the properties of LSPR. In general, we can observe several LSPR in the spectrum, and each LSPR represents LSP distribution on the metal NP surface: the strongest and most observable LSPR of NP represents the dipole mode whose (+) charge is on the one side of NP and (−) charge is on another side. The other weaker LSPR represents the higher-order modes that the charge distribution divided into four sides or more. In general, LSPR of NPs is determined by the type of metal, shape, and size of NPs.

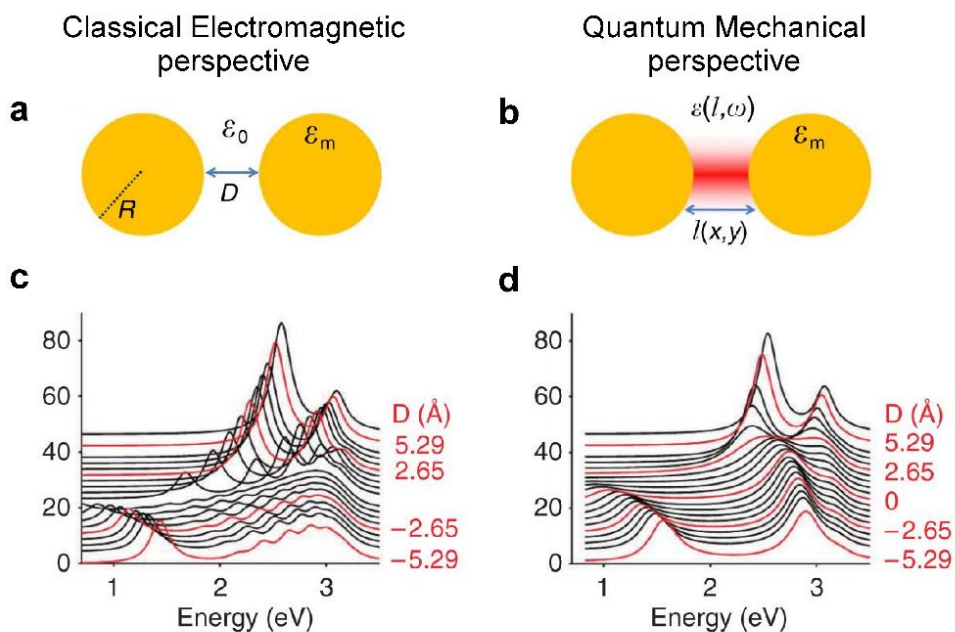


**Figure 1** The two perspectives of LSPR investigation.<sup>1</sup> The schematic diagram of (a) classical electromagnetic perspective and (b) quantum mechanical perspective. The spectrum of (c) classical electromagnetic perspective calculation and (d) quantum mechanical perspective calculation shows the opposite trend as the gap distance decreases. In quantum mechanical perspective, the calculation was done by setting an imaginary dielectric medium in the gap which can represent the tunneling effect properties. Figures are modified from the ref 1 with permission. Copyright © 2012, Springer Nature.

LSPR is used in many fields such as spectroscopy<sup>2-4</sup>, bioimaging<sup>5</sup>, drug delivery<sup>6</sup>, and sensor<sup>7-9</sup>. Especially, in the spectroscopy field, nanoparticles assembly with few nanometers gap is used. This is because the electric field in the gap is largely enhanced and this results in the enhancement of signal from the molecules in the gap. For example, the Raman scattering of molecules can be enhanced up to  $10^8$  (surface-enhanced Raman scattering, SERS) and even allows

us to measure the signal from the single molecule.

The electric field enhancement of nanoparticles assembly is determined by LSPR. Therefore, it is important to investigate LSPR with various factors and find out nanoparticles assembly which has appropriate LSPR for the experiment. In nanoparticles assembly, LSPR is not only affected by the type of metal, size, and shape of the NP but also by the gap distance, arrangement of NPs, and contact area. This is because new LSPR starts to arise from hybridization of original LSPR of the NPs when the gap distance becomes few nanometers. Therefore, if the arrangement of NPs changes, hybridization of LSPR changes and result in different LSPR.

The effects of the factors mentioned above have been largely investigated with both theoretical and experimental method. In these investigations, classical electromagnetic perspective was used with no quantum mechanical phenomenon such as tunneling effect and molecules were only regarded as dielectric medium (Figure 1a, c). However, in fact, there is a tunneling effect when the gap distance becomes few nanometers. The theoretical research<sup>1,10,11</sup> with this quantum mechanical perspective (Figure 1b, d) showed that hybridization of LSPR does not occur much as classical electromagnetic theory expected when the gap distance decreases because the tunneling effect makes the LSP charge smaller than expected. This phenomenon results in the reduction of LSPR red-shift which occurs as the gap distance decreases. Also, in this perspective, molecules play an additional role rather than dielectric medium because the interaction between NP and molecules can change the potential barrier and tunneling coefficient. Then, charge density on the metal surface and LSPR is different even though other

conditions are the same. This effect was reported with both theoretical<sup>12</sup> (Figure 2a) and experimental<sup>13</sup> research (Figure 2b). Especially, the experimental research showed that LSPR of the Au nanoparticle (AuNP)–molecule–template–tripped (TS) gold film junctions appears at different wavelength whether linkage of AuNP and gold film exists or not. The AuNP–biphenyl–4, 4' –dithiol (BPDT)–TS gold film junctions, which chemically link AuNP and TS gold film by two Au–S bonds in BPDT, show 50 nm blue–shift of LSPR compared to AuNP–biphenyl–4–thiol (BPT)–TS gold film junctions which cannot link two metal structures. This showed the indirect evidence of tunneling effect on LSPR.

The investigation of the tunneling effect on LSPR has difficulty because LSPR shift due to tunneling effect is small. Because there is heterogeneity of LSPR due to NP size, shape, arrangement, contact area, and gap distance which is larger than tunneling effect on LSPR, the difference of LSPR in two nanoparticles assemblies with different molecule mainly arise from LSPR heterogeneity, not by tunneling effect. Therefore, it is important to find the nanoparticles assembly with homogeneous shape, size, arrangement, contact area, and gap distance to investigate the tunneling effect on LSPR.

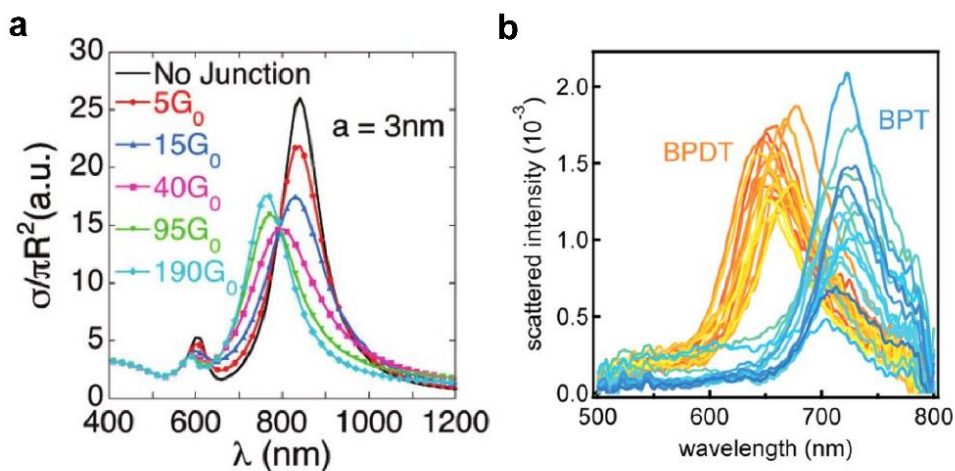


**Figure 2** (a) The previous calculation<sup>12</sup> and (b) experiment<sup>13</sup> research which showed the tunneling effect on LSPR. The  $G_0$  in (a) represents unit conductance and large conductance means high tunneling coefficient. Figures are modified from the ref 12, 13 with permission. Copyright © 2010 American Chemical Society, Copyright © 2014 American Chemical Society.

To reduce heterogeneity of LSPR and investigate the tunneling effect on the LSPR, we use the metal NP–molecule–AuTF junctions. Because probe molecules only exist between the NP and AuTF in this junction, only LSPR which engage in both NP and AuTF is considered and this ensures less heterogeneity. For examples, with sphere–like silver nanoparticle (AgNP), which is commonly used in this experiment, most of the AgNP–molecule–AuTF junctions has one strong LSPR appears near 550 nm called dipole mode.

## 1.2. The LSPR of the NP–molecule–AuTF

The LSPR of the NP–molecule–AuTF junction is affected by some factors: size of NP, gap distance, contact area and the refractive index of molecules. The effect of each factor was investigated in the previous study. Briefly, LSPR of the NP–molecule–AuTF junction shifts toward longer wavelength as the gap distance decreases<sup>14–16</sup> (Figure 3a), the refractive index of molecules increases<sup>16</sup> (Figure 3b), size of nanoparticle increases<sup>17,18</sup> (Figure 3c), and contact area increases<sup>15,17</sup> (Figure 3d). Especially, an Ag nanocube (AgNC)–molecule–AuTF junction, which is an extreme case of the increased contact area, shows the dipole mode LSPR in the near IR region and the higher order modes in the visible region<sup>15,16</sup> (Figure 4b).

We propose two methods to investigate the tunneling effect on LSPR: first, we observed the LSPR shift in one junction during a change of molecules by photoreaction (Figure 4a). Second, we removed the heterogeneity of LSPR which interrupts observation of tunneling effect by constructing well-defined single-crystalline junctions (Figure 4b).

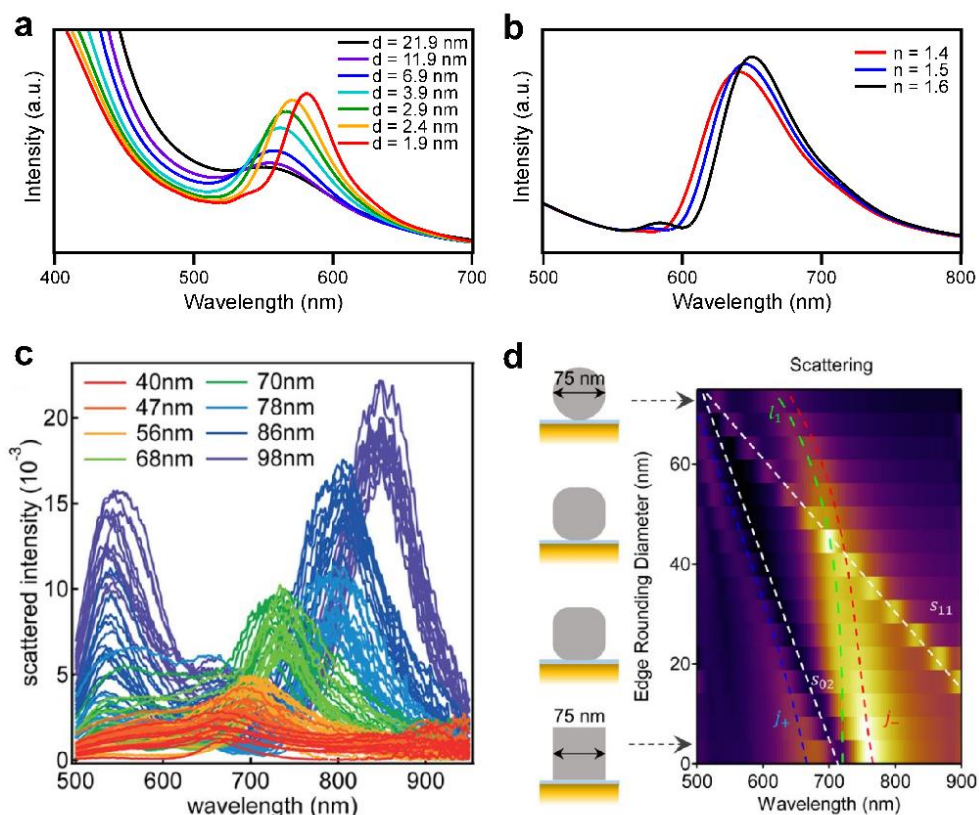


**Figure 3** LSPR spectrum (calculation) of the AgNP–molecule–AuTF junctions with (a) different gap distance (refractive index of molecule layer : 1.4, AuTF thickness : 30 nm) and (b) different refractive index of molecule layer (gap distance : 1.4 nm, AuTF thickness : 10 nm). The calculation was done by finite–difference time–domain (FDTD) method. The CRC model (Au), Palik model (Ag), and 1.4 (molecule layer) were used for the refractive index of each layer and diameter of AgNP is 80 nm. (c) The reported LSPR spectrum (experiment)<sup>18</sup> which showed the effect of nanoparticle size on LSPR in the AgNP–molecule–AuTF junctions. (d) The reported LSPR spectrum (calculation)<sup>15</sup> which showed the effect of the contact area of nanoparticles. Figure (c) and (d) are modified from the ref 18, 15 with permission. Copyright © 2016 American Chemical Society, Copyright © 2017 American Chemical Society.

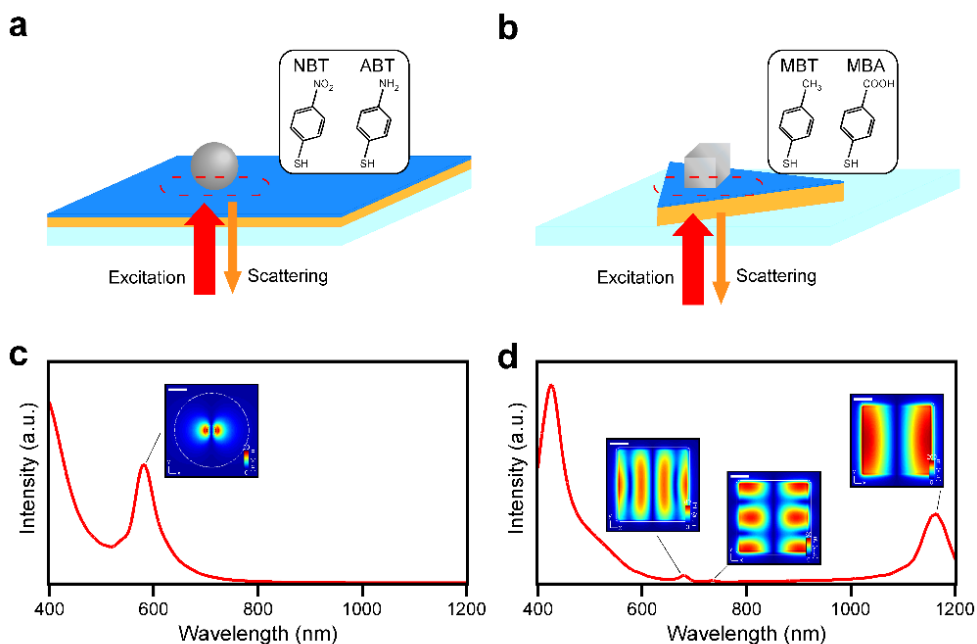


**Figure 4** The schematic diagram of the (a) AgNP–molecule–AuTF junctions and the (b) AgNC–molecule–Au platelet junctions used in this experiment. The black inset shows the structure of the molecules we introduced in each junction. 4–nitrobenzenethiol (NBT) and 4–aminobenzenethiol (ABT) were introduced in the AgNP–molecule–AuTF junctions, and 4–methylbenzenethiol (MBT) and mercaptobenzoic acid (MBA) were introduced in the AgNC–molecule–Au platelet junctions. (c) The calculated scattering spectrum of the AgNP–molecule–AuTF junctions shows one strong LSPR from dipole mode near 600 nm and (d) the calculated scattering spectrum of the AgNC–molecule–Au platelet shows one strong LSPR from dipole mode near 1200 nm and two weak LSPRs from higher order modes in the visible region. The insets show the electric field distribution of each LSPR on the top of the molecule layer (xy–plane, scalebar : 20 nm). The calculation was done by FDTD and the CRC model (Au), Palik model (Ag), and 1.4 (molecule layer) were used for the refractive index of each layer. The thickness of AuTF (10 nm) and Au platelet (30 nm), size of AgNP (diameter : 80 nm) and AgNC (side length : 80 nm), and gap distance (1.9 nm) were determined by the real value of each structure.

### 1.3. The dark-field spectroscopy

In this experiment, we used the dark-field spectroscopy which is a common technique to obtain the scattering spectrum. The scattering signal is hard to detect with normal bright-field spectroscopy because it is too small and overwhelmed by the reflection or transmission beam of the incident beam. In the dark-field spectroscopy, the reflection or transmission beam is blocked and the scattering signal is only detected. This is possible because the scattering signal radiates in every direction, unlike the reflection or transmission beam which follow the one allowed path.

In common transmission-type dark-field spectroscopy (Figure 5a, c), the doughnut-like white light is used for the incident beam and focused on the sample with a high-NA lens. Then, we can collect the scattering signal only in the center of the doughnut-like transmission beam with a low-NA objective lens.

However, this dark-field spectroscopy method has some restrictions: first, the efficiency of collection is low because a low-NA objective lens is essential to avoid the transmission beam. Second, because the field of view is wide, the scattering signal from other junctions nearby can interrupt detection of the targeted junction scattering signal. Although unwanted scattering signal is blocked with iris in the experiment, some of them still leak into the iris hole. The leaked scattering signal from other junctions is also problematic in data processing. The scattering signal detected from the targeted junction contains both of the scattering signals from the junction and the substrate. Because what we want is the scattering signal only from the targeted junction, we need to subtract the scattering from

the substrate which can be obtained at the position where is not a junction. However, because junctions nearby radiate their own scattering signal, the scattering signal of the substrate does not remain constant at junction position and substrate position. Therefore, it is impossible to eliminate the scattering from the substrate exactly.

These limitations of common dark-field spectroscopy can be improved with the supercontinuum laser which is the only broadband light source that can be focused on the sample surface. In this confocal dark-field spectroscopy set-up, the other junctions do not radiate the scattering signal because the incident beam is focused on the targeted junction and there is no light source for the other junctions. To construct a confocal dark-field set-up, we modified the confocal dark-field set-up with reflection-type microscopy which was reported in the previous work<sup>18</sup> (Figure 5b, e). In the previous work, they made the doughnut-like incident beam with supercontinuum laser by adjusting the beam size with collimation lenses and a beam block. Then they blocked the reflection beam with iris and detected the scattering signal in the center of the doughnut. However, in our experiment, we use the original beam from the supercontinuum laser as the incident beam and block the reflection beam with the beam block (Figure 5c, f). Then, we can detect the scattering signal in a high-NA doughnut-like region with the suitable size of the beam block. This modification permits some improvements compared to the previous version of the confocal dark-field spectroscopy: first, because we use no collimation lenses in front of an objective lens, we can eliminate the chromatic aberration of the incident beam. Also, by using the achromatic lens for focusing into the Raman spectrometer, we minimized the chromatic aberration in

the total system. Second, the collection efficiency of the scattering signal is improved. This is because the scattering signal radiates into a high-NA region more than low-NA region. Therefore detection in a doughnut-like region, which is a high-NA region, ensures us to collect more scattering signal rather than detection in a low-NA center region.

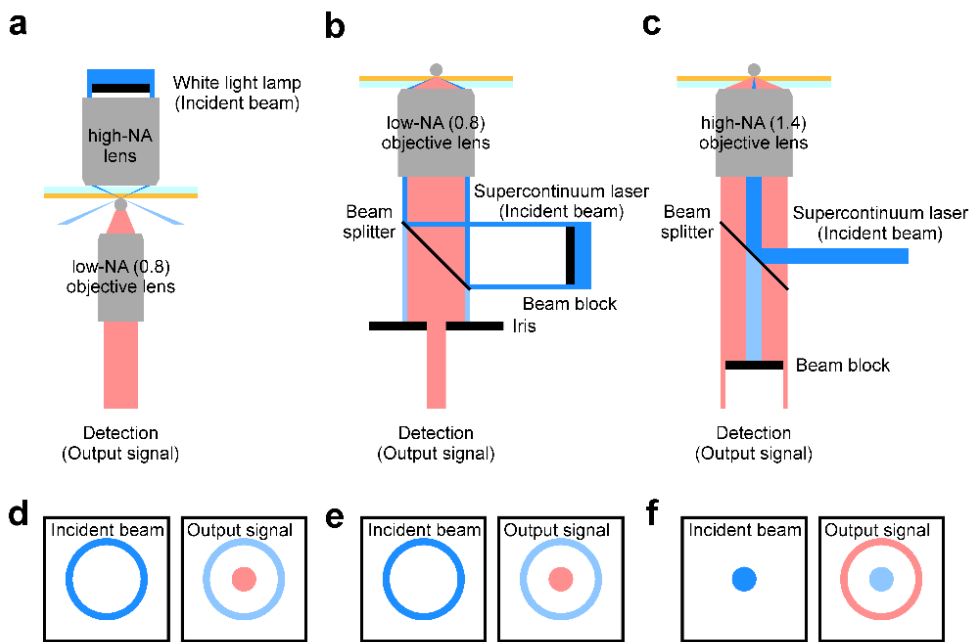


**Figure 5** The schematic diagram (a, b, c) and a cross-section of the output signal (d, e, f) of the (a, d) general dark field set-up, (b, e) the reported confocal dark-field set-up<sup>18</sup>, and (c, f) the home-built confocal dark-field set-up. The blue line represents the incident beam, the light-blue line represents the reflection beam, and the light-red line represents the scattering signal from the sample.

## Chapter 2. Experimental Set-up

The home-built confocal dark-field set-up was constructed to investigate the scattering signal of the NP-molecule-AuTF junctions. The supercontinuum laser was used as broadband light source and the original beam from the laser with no size adjustment was entered into the center of a high-NA objective lens. The circle-like beam block with 7.5 nm diameter was used to block the reflection beam and the scattering signal in a high-NA doughnut-like region is focused into the Raman spectrometer.

To obtain the scattering spectrum of the NP-molecule-AuTF junctions, four signals were needed to be obtained: first, the scattering signal of the NP-molecule-AuTF junction position was needed. Second, the scattering signal of the substrate which was obtained at the different position in the same sample with no NPs was needed to eliminate the scattering from the substrate. In general, the distance between the junction position and the substrate position was maintained as 1  $\mu\text{m}$ . Third, the incident light source was measured on the clean glass without beam block. This is because the scattering signal is proportional to the intensity of the incident beam and the light source has different intensity along wavelength. Therefore, normalization by the intensity of light source was needed to obtain the scattering spectrum. Finally, the dark-current signal, which is the background signal of a detection device which was obtained without any light source, was needed. Because the dark-current signal exists as background in every signal, we need to subtract the dark-current signal from three to other signals to obtain the actual

signals. Then, the scattering spectrum can be calculated with the equation  $I_{\text{dark-field}}(\lambda) = (I_{\text{junction}}(\lambda) - I_{\text{substrate}}(\lambda)) / (I_{\text{lightsource}}(\lambda) - I_{\text{dark-current}}(\lambda))$ .

The home-built confocal SERS set-up was conjugated with the confocal dark-field set-up to detect the SERS signal of the same junction simultaneously. The HeNe laser was used as the excitation light source for SERS detection. The Rayleigh scattering which overwhelms the Raman scattering signal was blocked with Raman notch filter.

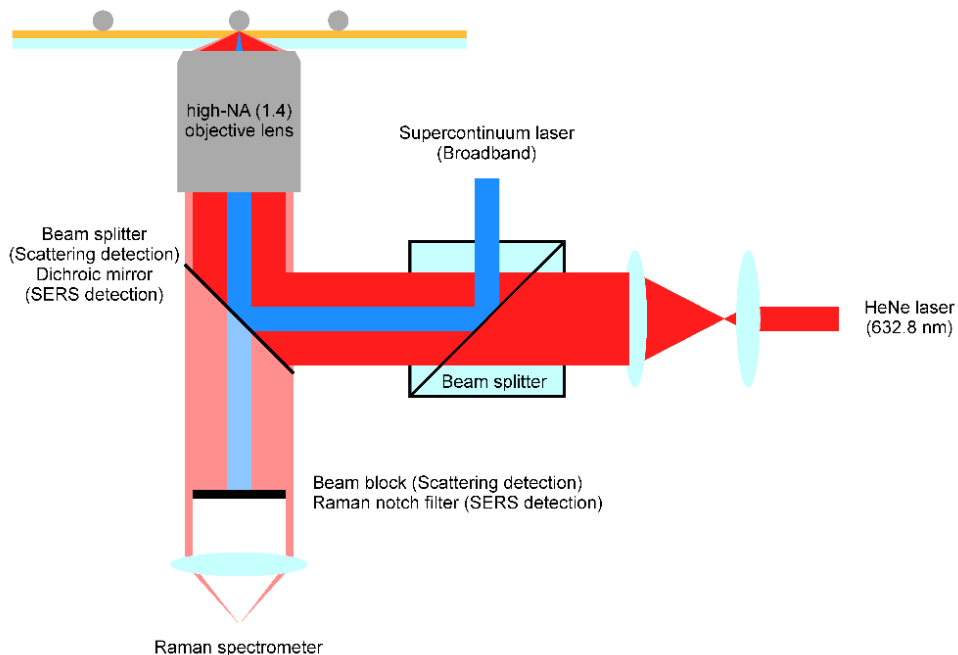


**Figure 6** The schematic diagram of the home-built confocal dark-field/SERS set-up. The blue line represents the incident beam of the supercontinuum laser for the dark-field spectroscopy and the red line represents the incident beam of the HeNe laser for the SERS spectroscopy. Two incident light sources were correlated with 5 : 5 broadband beam splitter. The light-blue line represents the reflection beam of the supercontinuum laser and the light-red line represents the scattering signal from the sample. The sphere-like beam block was used to block the reflection beam of supercontinuum laser in front of the Raman spectrometer. This was substituted into the Raman notch filter to block the strong Rayleigh scattering when we obtained the SERS spectrum.

# Chapter 3. Investigation of tunneling effect on LSPR : photoreduction of NBT

## 3.1. The photoreduction of NBT

To change the molecule in the junction and observe the tunneling effect on LSPR, we used the well-known photoreduction of NBT. The previous studies<sup>2,4</sup> showed that NBT is reduced to ABT by obtaining 6 electrons when there is light. Also, it was reported that there is side reaction that NBT is reduced to 4, 4' - dimercaptoazobenzene (DMAB) and then DMAB is reduced to ABT again.

The one way to investigate this reaction is using SERS spectroscopy<sup>2,4</sup>. This can be possible because the monochromatic laser can be acted as the light source for photoreduction and excitation laser source for SERS measurement. Figure 7b shows the SERS spectrum of related molecules. The main peak of NBT is symmetric N-O stretching ( $\nu_s(NO)$ ,  $1329\text{ cm}^{-1}$ ) which is the largest. Because this peak does not appear in ABT, we can know whether the reaction occurs or not by the intensity of  $\nu_s(NO)$ . Especially, the previous study<sup>2</sup> with the AgNP-NBT-AuTF junctions, which we used in this investigation, showed the real-time SERS spectrum change of almost 30 molecules in the junction (expected by FDTD calculation) (Figure 7c). The main change of the SERS spectrum is the decay of  $\nu_s(NO)$ , which means the reduction of NBT. The formation of ABT is hardly observed by SERS spectrum because the

two main peaks of ABT appear at the similar wavenumber of NBT peaks and the formation of DMAB is easily observed by the new SERS peaks arise after the 10 s. However, by calculating from the SERS peak ratio, it was reported that more than 90 % of NBT becomes ABT and less than 10 % of NBT becomes DMAB. Therefore, we can expect most of NBT becomes ABT and LSPR shift after the photoreduction is originated from the difference between ABT and NBT, not DMAB and NBT.

Using NBT photoreduction in the AgNP–molecule–AuTF junctions has some advantages: first, because the amine group of ABT can make a bond with Au atom, this reaction can change the potential barrier and the tunneling coefficient. Second, we can simultaneously check whether NBT is reduced to ABT or not with the SERS spectrum. Third, NBT has no conformation uncertainty as dithiol does. The junction using dithiol has conformation uncertainty because we cannot convict that two thiol groups are really connected to different metal structures.

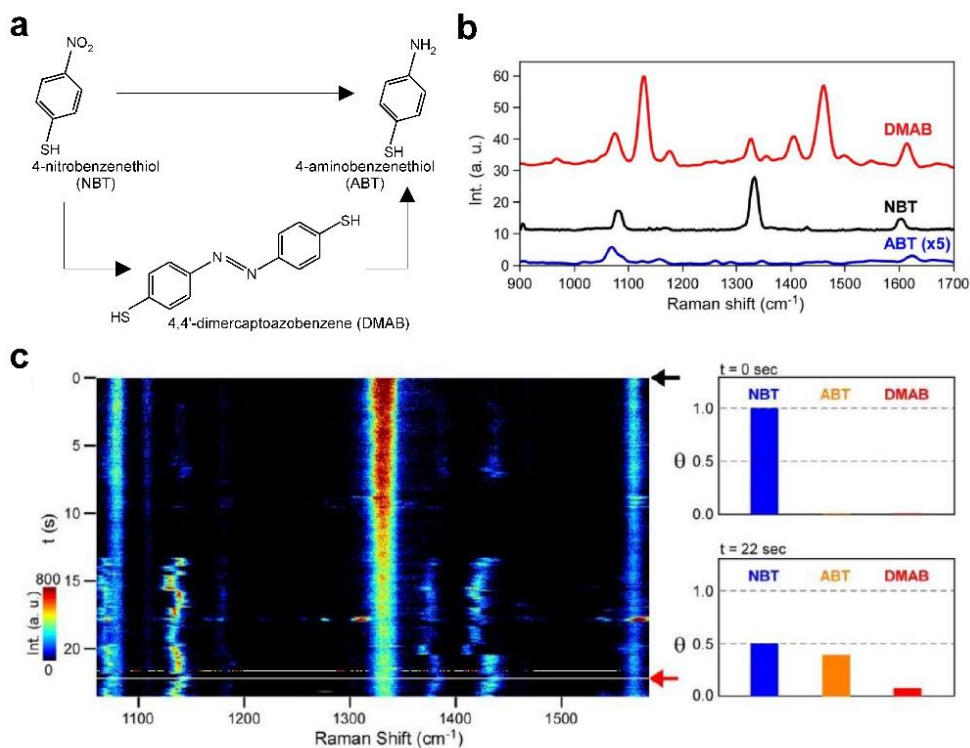


**Figure 7** (a) The schematic diagram of NBT photoreduction and (b) the SERS spectrum of each molecule<sup>2</sup>. (c) The real-time SERS spectrum obtained in the AgNP–NBT–AuTF junctions shows that we can track the reaction with the intensity of  $\nu_s(\text{NO})$ . The graph on the right side of (c) implies that most (> 90 %) of NBT is reduced to ABT rather than DMAB.<sup>2</sup> Figure (b) and (c) are modified from the ref 2. Copyright © 2016 American Chemical Society.

### 3.2. The LSPR shift during NBT reduction

The AgNP–NBT–AuTF junctions were constructed by the following procedure: NBT self–assembled monolayer was formed on the surface of 10 nm AuTF, and the AgNP was drop–casted on the NBT–AuTF surface. To observe the LSPR shift of the AgNP–NBT–AuTF junctions, the scattering spectrum was first obtained with home–built confocal dark–field spectroscopy. Then, NBT in the junction was reduced to ABT with the HeNe laser irradiation and the SERS spectrum was obtained simultaneously. The irradiation was stopped when the intensity of  $\nu_s(NO)$  of the junction decreases under 1/3 of the initial intensity. Then, the scattering spectrum of the same junction was obtained again.

The scattering spectrum of the AgNP–NBT–AuTF junctions was obtained (Figure 8b). In most of the junctions, LSPR appears around the 550 nm which is well–matched with the simulation. However, there was heterogeneity of LSPR which we cannot neglect. This arose mostly from the heterogeneity of NPs and the contact area.

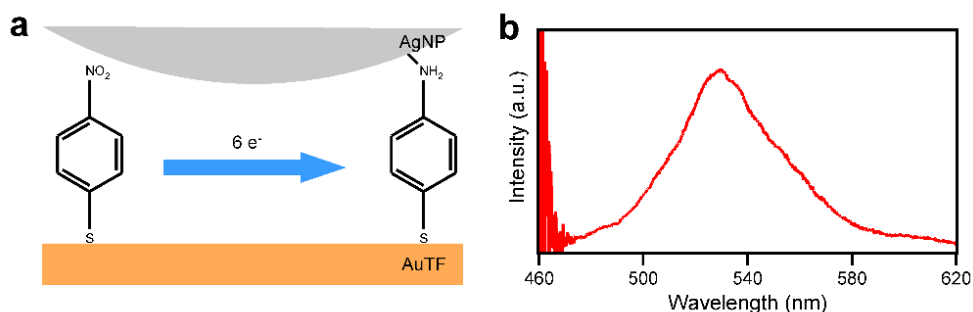


**Figure 8** (a) The schematic diagram of the change in the AgNP–NBT–AuTF junctions and (b) the scattering spectrum of the junction.

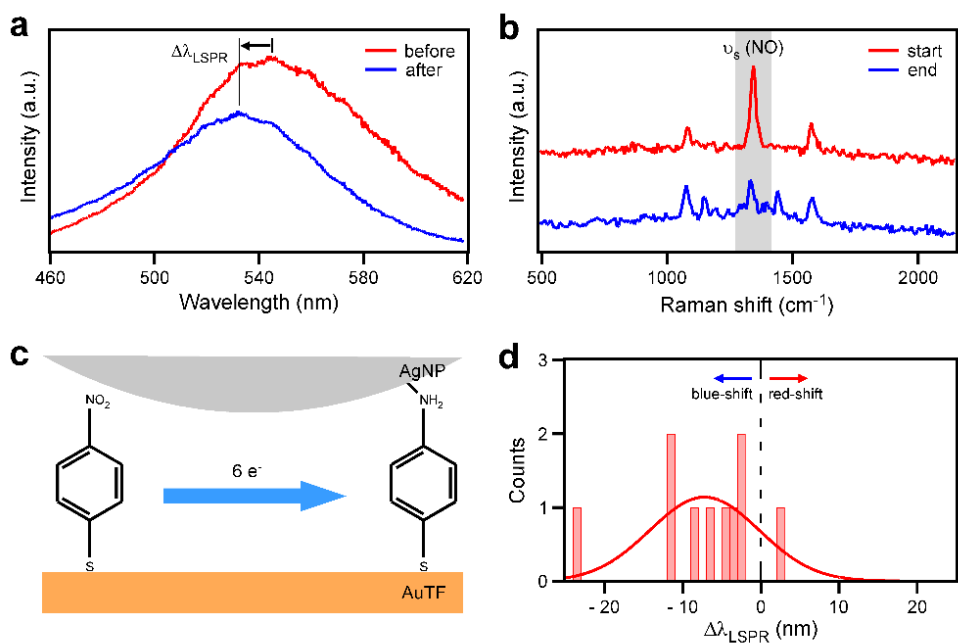


**Figure 9** (a) The scattering spectrum of the AgNP–NBT–AuTF junctions before (red) and after (blue) the HeNe laser irradiation in one junction. (b) The SERS spectrum obtained during the HeNe laser irradiation (start : red, end : blue) in the same junction. (c) The schematic diagram of the molecular change in the AgNP–NBT–AuTF junction during the HeNe laser irradiation. (d) The histogram of  $\Delta\lambda_{LSPR}$  in 10 junctions. The LSPR shift was calculated by the equation  $\Delta\lambda_{LSPR} = \lambda_{ABT} - \lambda_{NBT}$ . The peak position was obtained by measuring the maximum position of the smoothed spectrum. The smoothing was done by Gaussian-type smoothing with  $\sigma = 15$ . The average peak shift and standard deviation obtained by Gaussian fitting is 7.2 nm blue–shift and 7.0 nm.

Figure 9a shows the shift of LSPR when NBT is reduced to ABT molecule. The two spectrums were obtained in the same junction to eliminate the effect of junctions heterogeneity. In most of the junctions, LSPR shifts toward shorter wavelength as photoreduction occurs. The SERS spectrum of the junction was used to check the reduction of NBT molecules to ABT molecules. The intensity of

$v_s(NO)$  decreases during the reaction and becomes at least 1/3 of initial peak intensity at the end of the reaction (Figure 9b) in all junctions. The initial SERS spectrum (Figure 9b red), which measured right after the measurement of the scattering signal (Figure 9a red) shows that negligible NBT molecules are reduced to ABT by supercontinuum laser. This is also verified with the experiment observing real-time scattering spectrum with supercontinuum laser. In this experiment, we observed the real-time (time interval : 50 ms) scattering spectrum at the junction for 5 minutes (Figure 10a). Although the scattering spectrum changes during the measurement temporarily (Figure 10b), the SERS spectrum measured after the scattering measurement shows that nearly no NBT reduced to ABT (Figure 10c).

The histogram of  $\Delta\lambda_{LSPR}$  is presented in the Figure 9d. Although data is insufficient to observe the distribution of  $\Delta\lambda_{LSPR}$ , this histogram clearly shows that blue-shift of LSPR occurred in most of the junctions (average  $\Delta\lambda_{LSPR} = 7.2$  nm blue-shift,  $\sigma = 7.0$  nm). This implies that peak shift of LSPR is not special but general phenomenon when NBT reduction occurs. Also, in the AgNP-MBT-AuTF junctions whose molecules do not change, smaller  $\Delta\lambda_{LSPR}$  was observed (average  $\Delta\lambda_{LSPR} = 2.5$  nm blue-shift,  $\sigma = 6.0$  nm) with the same laser power and irradiation time condition. This shows that additional blue-shift in the AgNP-NBT-AuTF junctions ( $\sim 5$ nm) is originated from the difference between the AgNP-NBT-AuTF junctions and the AgNP-ABT-AuTF junctions.

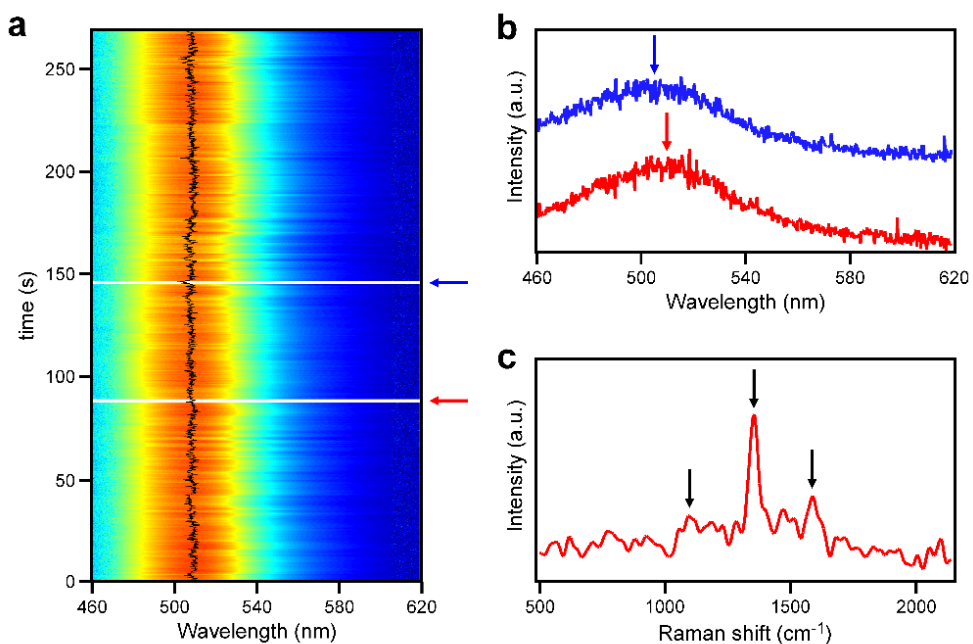


**Figure 10** (a) The real-time scattering spectrum during the supercontinuum laser irradiation. Each spectrum was smoothed with the Gaussian-type smoothing ( $\sigma = 20$ ). The black line shows the maximum point of the smoothed spectrum. (b) The scattering spectrum profile shows a temporal shift in one junction. The spectrum below (red) shows the scattering spectrum profile at the time pointed with a red arrow in (a) and the spectrum above (blue) shows the scattering spectrum profile at the time pointed with a blue arrow in (a). The colored arrow in b shows the maximum point of each spectrum. (c) The SERS spectrum after the supercontinuum laser irradiation shows that the negligible number of NBT is reduced. The black arrows indicate the three main SERS peaks of NBT.

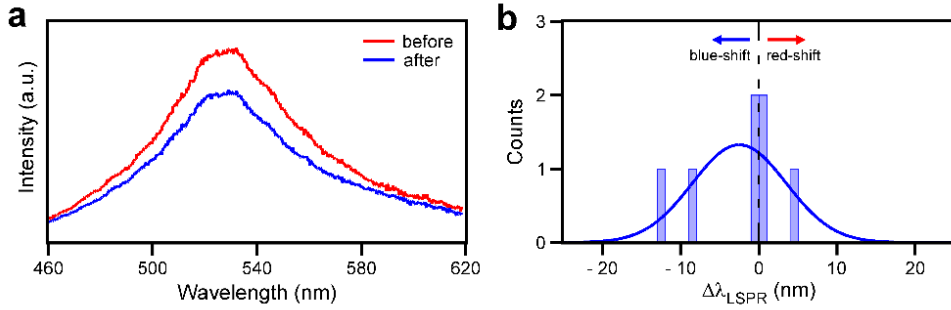


**Figure 11** (a) The scattering spectrum of the AgNP–MBT–AuTF junction. The power of the HeNe laser and irradiation time was maintained similar to the AgNP–NBT–AuTF junction experiment. (b) The histogram of  $\Delta\lambda_{LSPR}$  in 7 junctions. The determination of peak position and  $\Delta\lambda_{LSPR}$  is same as the method presented in Figure 9.

There are four possible factors which can result in LSPR shift during the experiment: welding of the NPs, change of refractive index, charging effect and tunneling effect. First, NPs can weld during the laser irradiation. If NPs welds, the contact area becomes larger and results in the red–shift of LSPR<sup>19,20</sup>. The previous research with 477 nm laser<sup>20</sup> (Figure 12a) showed that this phenomenon can possibly occur in our experiment condition. However, the blue–shift which observed in our experiment is clearly opposed to the effect of welding. Also, the nearly zero  $\Delta\lambda_{LSPR}$  in the AgNP–MBT–AuTF junctions shows that the  $\Delta\lambda_{LSPR}$  in the AgNP–NBT–AuTF junctions does not originated from the structural change. Therefore, we can conclude that the welding does not affect LSPR in our experiment condition.

Second, the difference between refractive index of NBT ( $n = 1.62$ <sup>21</sup>) and ABT ( $n = 1.665$ <sup>22</sup>) can make LSPR difference between the AgNP–NBT–AuTF junctions and the AgNP–ABT–AuTF

junctions. It is well-known that LSPR appears at longer wavelength when the refractive index becomes larger. Therefore, the AgNP-ABT-AuTF junctions show LSPR at a slightly longer wavelength than the AgNP-NBT-AuTF junctions (Figure 12b). However, because this also shows the opposite tendency to our experiment result, we can conclude that there is another factor which shifts LSPR toward shorter wavelength.

Third, LSPR can change when the metal structure is charged. Due to the previous study<sup>23,24</sup>, less than 2.5 nm red-shift occurs when electron density of 20 nm AgNP decreases by 1%. However, because the number of electrons which is needed for NBT photoreduction is 6 and the number of NBT molecules in the AgNP-NBT-AuTF junctions is 30, the maximum change of the number of electrons is 180. This is a negligible number compared to the total number of electrons in the 80 nm AgNP ( $2.8 \times 10^6$ ). This infers that  $\Delta\lambda_{LSPR}$  originated from the electron loss is negligible. Therefore, we can conclude that electron loss during the photoreduction is not the reason for LSPR blue-shift.

Finally, the change of tunneling coefficient due to molecule change can shift LSPR. Because the amine group of ABT can form N-Au bond, the potential barrier of the AgNP-ABT-AuTF junctions is lower than that of the AgNP-NBT-AuTF junctions. This results in a decrease of charge density on the surface and blue-shift of LSPR. Therefore, during the photoreduction of NBT, tunneling coefficient becomes larger due to ABT formation and LSPR shifts toward shorter wavelength.

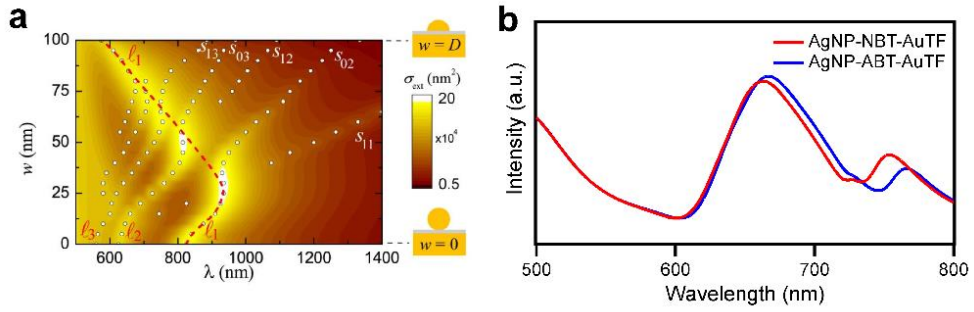


**Figure 12** (a) The calculated LSPR spectrum<sup>19</sup> with the different contact area. The laser irradiation can weld the AgNP and shift LSPR toward longer wavelength. (b) The calculated LSPR spectrum of the AgNP–molecule–AuTF junction with reported refractive index (NBT : 1.62, ABT : 1.665). Figure (a) is modified from the ref 19 with permission. Copyright 2015 by the American Physical Society.

By considering the possible factors and each effect which can shift LSPR of the AgNP–NBT–AuTF junctions, we can explain the observed blue–shift of LSPR with tunneling effect. The other factors cannot explain LSPR shift because the effect is negligible and even opposite to the observed phenomenon. Even though more experiment is needed to observe the exact tendency of LSPR shift, but this phenomenon ensures us to adjust LSPR of the total metal structure simply by changing the molecules.

# Chapter 4. Investigation of tunneling effect on LSPR : single-crystalline junction

## 4.1. Synthesis of Au platelet

To construct the AgNP–molecule–AuTF junctions with well-defined single-crystalline structures, we substituted AgNP with the Ag or Au nanocube and AuTF with the micron-size single-crystalline Au platelet. Both of structures have well-defined  $\{1\ 1\ 1\}$ -facet and atomically flat surface. The synthesis method of each structure was developed in the previous studies. Especially, single-crystalline micron-size Au platelet was synthesized with several methods using poly(diallyldimethylammonium chloride) (PDDA)<sup>25</sup>, cetyltrimethylammonium bromide (CTAB)<sup>26,27</sup> or polyvinylpyrrolidone (PVP). The common mechanism of platelet growth is similar to that of other nanostructures<sup>28</sup>. First, small seed NPs are generated by the reduction of Au<sup>3+</sup> ion. Then, surfactant molecules are attached on the surface of seed NPs. In this step, the surfactant molecules prefer to be attached on  $\{1\ 1\ 1\}$ -facet in the condition of platelet synthesis. Then, when new Au<sup>3+</sup> ion reduces, this Au atom is attached on the side of platelet rather than  $\{1\ 1\ 1\}$ -facet because of surfactant. Therefore, the seed NPs grow in the direction of the plane and finally become platelet. In this experiment, we used the fast, simple synthesis method which was developed by Luo<sup>25</sup>. In this method, HAuCl<sub>4</sub> (100  $\mu$ L, 0.0486 M), salicylic acid (50  $\mu$ L, 0.292 M), and PDDA (112.5  $\mu$ L, 0.128 M) aqueous solutions were

used for gold source, a reducing agent, and surfactant. Each solution was mixed together sequentially and then diluted to 5 mL with water. For platelet growth, this solution was heated at 100 °C for 5 minutes. In our experiment, some of the steps in this synthesis scheme were modified.

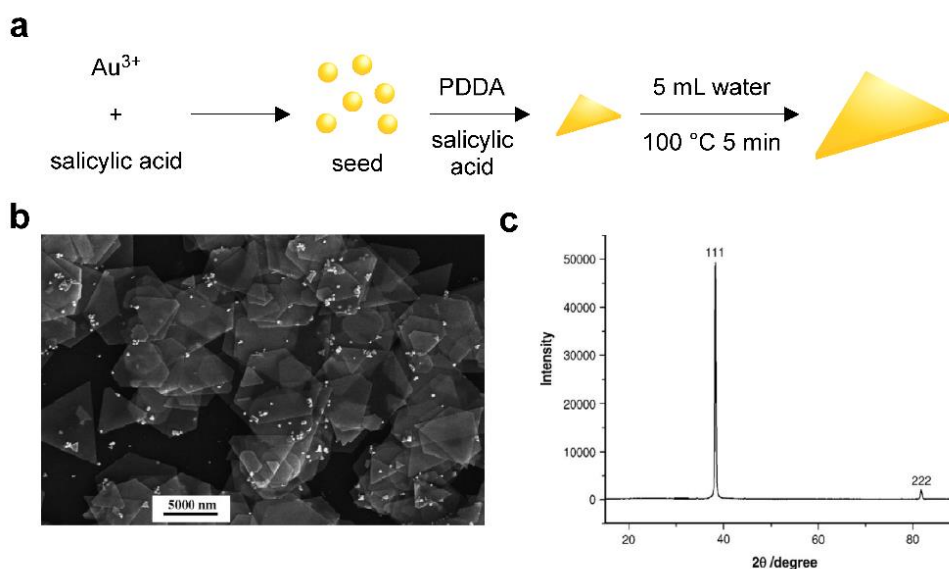


**Figure 13** (a) The schematic diagram of reported atomically flat single-crystalline micro-size Au platelet synthesis.<sup>25</sup> The (b) SEM image and the (c) XRD pattern shows the formation of single-crystalline Au platelet. Figure (b) and (c) are modified from the ref 25 with permission. Copyright © 2006 Elsevier B. V.

## 4.2. Fabrication of single-crystalline junction

The various modification of single-crystalline micron-size Au platelet synthesis method was tried to find the appropriate condition. First, changing the sequence of reactant addition was tried and we found out that the sequence reported in the previous report<sup>25</sup> was the best. Second, the concentration of the reactant solution was controlled. If the concentration of all reactants (HAuCl<sub>4</sub>, salicylic acid, PDDA) was diluted, the height and size of the Au platelets decrease. Also, there was no correlation between the molar ratio of salicylic acid/PDDA and the properties of Au platelets. However, by the previous studies and mechanism of synthesis<sup>28</sup>, we expected that the height and size of Au platelet decrease as the molar ratio of salicylic acid/PDDA decreases. This unexpected result can be explained by the reaction temperature. The reaction temperature reported was 100 °C which is a high temperature in the aqueous condition. Especially, the salicylic acid solution was problematic because it needed to be heated as 100 °C to make the reported concentration of the solution. However, because water vaporized a lot at this temperature, the concentration of salicylic acid uncontrollable. The uncontrollable concentration results in the lack of reproducibility and tendency. Therefore, we need to fix the concentration of the salicylic acid solution to improve reproducibility and tendency. This was possible by making a saturated solution at 100 °C. The amount of saturated solution to be added was determined to contain the same total mole of salicylic acid. Also, high temperature, which makes reaction fast, reduces the reproducibility. This is because a small change in the step of reactant addition such as mixing degree or time

interval between three reactant addition results in large difference because the reaction is too fast. To overcome this limitation, we first maintained the temperature at 75 °C, relatively low temperature, and then raised the temperature to 100 °C. Because this reduces the initial reaction speed, change in the step of reactant addition results in less change of the products. Also, because the height of Au platelet is determined in the first step, decreasing the temperature made us to synthesis height-controlled Au platelet. Third, the stirring degree of the solution was controlled. Without mixing, Au platelets had a high heterogeneity of height and size in one sample. However, with the mixing of reaction solution made us get Au platelet with relatively low heterogeneity.

The best condition to synthesize atomically flat single-crystalline micron-size Au platelet was to use aqueous  $\text{HAuCl}_4$  solution (0.0486 M, 100  $\mu\text{L}$ ), aqueous salicylic acid solution (saturated solution at 75 °C, 116  $\mu\text{L}$ ) and aqueous PDDA solution (0.128 M, 113  $\mu\text{L}$ ). Each solution was sequentially added into a warm vial. The time interval between the addition of solutions was maintained as short as possible. After adding three solutions, 5 mL of warm deionized water was added to dilute the mixture. The mixture was located in 75 °C water bath for 1 minute and moved into 100 °C water bath. After 5 minutes in 100 °C water bath, the mixture was cooled in room temperature condition. During the synthesis, the temperature was controlled by a water bath on a heating mantle with a temperature controller and all mixture was gently mixed with a magnetic stirring bar. After all synthesis steps, golden precipitates were observed in the vial. These golden precipitates were washed with deionized water for twice and ethanol

for once by sonication ( $\sim 1$  minute) and centrifuge ( $\sim 2000$  rpm,  $\sim 5$  minutes). The size, height and topographical properties of synthesized micron-size Au platelet were measured by atomic force microscopy (AFM). To use micron-size Au platelet as the substitute of AuTF, washed micron-size Au platelet was drop-casted on the cover glass cleaned with Piranha solution and RCA solution.

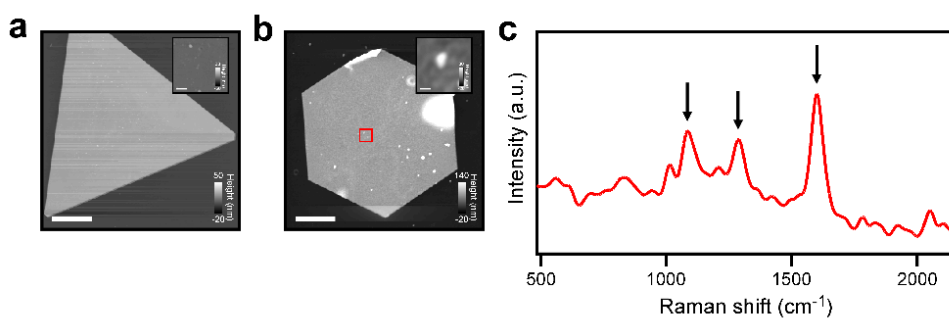


**Figure 14** (a) The AFM topography of synthesized atomically flat single-crystalline micron-size Au platelet (scale bar : 2  $\mu\text{m}$ ) and the magnified AFM topography of Au platelet surface (inset, scale bar : 200 nm). (b) The AFM topography of constructed the AuNC-BPT-Au platelet junction (scale bar : 4  $\mu\text{m}$ ) and the magnified AFM topography of the junction in the red box (inset, scale bar : 200 nm). (c) The SERS spectrum of junction showed that surfactant of Au platelet and AuNC effectively removed by wash process. The black arrows indicate the three main SERS peaks of BPT.

Figure 14a shows the AFM topography of Au platelet which was synthesized in the modified method. By this synthesis method, most of the synthesized Au platelets are large enough (side length  $> 5 \mu\text{m}$ ) to substitute the AuTF and the average height of Au platelets was about 30 nm which is thinner than the penetration length of light in the Au. This fact allows us to use a high-NA objective lens with a transmission-type microscope, which ensures high collection efficiency.

Because the synthesized Au platelet has surfactant (PDDA) on their surface, target molecules cannot adsorb on the surface without the surfactant removal process. The surfactant removal process differs from the type of surfactant. PDDA, the surfactant of Au platelet, was removed enough to form a self-assembled monolayer of thiol molecules by wash with ethanol and methanol. The NCs, which was used as the substitute of NPs, also has surfactant on their surface to control their shape. In our experiment, we used purchased silver nanocube (AgNC, nanoComposix) with PVP and purchased gold nanocube (AuNC, Nanopartz) with CTAB. In the case of AgNC, PVP was removed by ten times wash with ethanol and methanol and then put into the thiol solution to substitute surfactant with thiols. There are other PVP removal methods reported<sup>29,30</sup>, such as reducing with  $\text{NaBH}_4$ <sup>31,32</sup>, but wash with organic solvent was the best solution to remove surfactant with no surface damage and aggregation formation. In the case of AuNC, CTAB was removed by three times wash with methanol and put into methanolic thiol solution. To find out whether surfactant was removed or not, the SERS spectrum of the AuNC-BPT-Au platelet was obtained (Figure 14c). Also, to remove the possibility that the SERS signal arises from the AuNC-AuNC

junctions, the AFM topography of the junction was obtained (Figure 14b). Because the three main SERS peaks were observed in the SERS spectrum and no AuNC dimers were observed around the junction position, we concluded that the SERS signal was really from the AuNC–BPT–Au platelet junctions and surfactant was removed. Also, by comparing the SERS signal with the AuNP–BPT–Au platelet, AuNP–BPT–AuTF, AuNC–BPT–AuTF junctions, we concluded that the surfactant was sufficiently removed to enhance the Raman signal as the systems which have no surfactant.

We need the additional experiment to investigate the tunneling effect on LSPR in the AuNC–molecule–Au platelet junctions. The experiment will be performed with MBT and MBA. Because the carboxylic acid group of MBA can coordinate the Au atom in AuNC, tunneling coefficient in two junctions are different. Also, because the higher order mode LSPR, which appears in the visible region in the AuNC–molecule–Au platelet junctions, is more affected by the surrounding condition than the dipole mode LSPR, the sensitive LSPR shift is expected as the tunneling coefficient changes. Therefore, we expect an effective investigation of the tunneling effect on LSPR in the AuNC–molecule–Au platelet junctions.

## Conclusion

To sum, we investigated the tunneling effect on LSPR of the NP–molecule–AuTF junctions. To eliminate the structural heterogeneity of the junctions, which interrupts the observation of LSPR difference due to a molecule, we used two different systems. First, we observed the LSPR shift in one AgNP–NBT–AuTF junction when NBT is reduced to ABT. The blue–shift of LSPR was observed in general and this was only explained by the tunneling coefficient change due to molecules change. Although the additional experiment is needed to observe the exact distribution of LSPR shift, this phenomenon ensures the possibility to modify LSPR of the metal structure by changing molecules in the surroundings. Second, we constructed the metal structure with atomically flat single–crystalline micron–size Au platelet and well–defined NCs. The formation of the AuNC–molecule–Au platelet was checked by the SERS spectrum and the AFM topography. The additional experiment will be performed with MBT and MBA. This system is expected to have larger sensitivity than the AgNP–molecule–AuTF junctions because the higher order mode is measured in the visible region.

## Bibliography

1. Esteban, R., Borisov, A. G., Nordlander, P. & Aizpurua, J. Bridging quantum and classical plasmonics with a quantum-corrected model. *Nat. Commun.* **3**, 825–829 (2012).
2. Choi, H. K. *et al.* Metal-Catalyzed Chemical Reaction of Single Molecules Directly Probed by Vibrational Spectroscopy. *J. Am. Chem. Soc.* **138**, 4673–4684 (2016).
3. Shin, H. H. *et al.* Frequency-Domain Proof of the Existence of Atomic-Scale SERS Hot-Spots. *Nano Lett.* **18**, 262–271 (2018).
4. Choi, H. K., Lee, K. S., Shin, H. H. & Kim, Z. H. Identification of the First Elementary Step in the Photocatalytic Reduction of Nitrobenzenethiols on a Metallic Surface. *J. Phys. Chem. Lett.* **7**, 4099–4104 (2016).
5. Wolfbeis, O. S. An overview of nanoparticles commonly used in fluorescent bioimaging. *Chem. Soc. Rev.* **44**, 4743–4768 (2015).
6. Ghosh, P., Han, G., De, M., Kim, C. K. & Rotello, V. M. Gold nanoparticles in delivery applications. *Adv. Drug Deliv. Rev.* **60**, 1307–1315 (2008).
7. Nath, N. & Chilkoti, A. Label-free biosensing by surface plasmon resonance of nanoparticles on glass: Optimization of nanoparticle size. *Anal. Chem.* **76**, 5370–5378 (2004).
8. Chen, P. & Liedberg, B. Curvature of the localized surface plasmon resonance peak. *Anal. Chem.* **86**, 7399–7405 (2014).

9. Chen, P., Tran, N. T., Wen, X., Xiong, Q. & Liedberg, B. Inflection Point of the Localized Surface Plasmon Resonance Peak: A General Method to Improve the Sensitivity. *ACS Sensors* **2**, 235–242 (2017).
10. Zhu, W. *et al.* Quantum mechanical effects in plasmonic structures with subnanometre gaps. *Nat. Commun.* **7**, 11495 (2016).
11. Marinica, D. C., Kazansky, A. K., Nordlander, P., Aizpurua, J. & Borisov, A. G. Quantum plasmonics: Nonlinear effects in the field enhancement of a plasmonic nanoparticle dimer. *Nano Lett.* **12**, 1333–1339 (2012).
12. Pérez–González, O. *et al.* Optical spectroscopy of conductive junctions in plasmonic cavities. *Nano Lett.* **10**, 3090–3095 (2010).
13. Benz, F. *et al.* Nanooptics of molecular–shunted plasmonic nanojunctions. *Nano Lett.* **15**, 669–674 (2015).
14. Huang, S. *et al.* Ultrasmall Mode Volumes in Plasmonic Cavities of Nanoparticle–On–Mirror Structures. *Small* **12**, 5190–5199 (2016).
15. Chikkaraddy, R. *et al.* How Ultranarrow Gap Symmetries Control Plasmonic Nanocavity Modes: From Cubes to Spheres in the Nanoparticle–on–Mirror. *ACS Photonics* **4**, 469–475 (2017).
16. Zhang, S., Bao, K., Halas, N. J., Xu, H. & Nordlander, P. Substrate–induced Fano resonances of a plasmonic nanocube: A route to increased–sensitivity localized surface plasmon resonance sensors revealed. *Nano Lett.* **11**, 1657–1663 (2011).

17. Huang, Y., Ma, L., Li, J. & Zhang, Z. Nanoparticle–on–mirror cavity modes for huge and/or tunable plasmonic field enhancement. *Nanotechnology* **28**, 105203 (2018).
18. Benz, F. *et al.* SERS of Individual Nanoparticles on a Mirror: Size Does Matter, but so Does Shape. *J. Phys. Chem. Lett.* **7**, 2264–2269 (2016).
19. Tserkezis, C. *et al.* Hybridization of plasmonic antenna and cavity modes: Extreme optics of nanoparticle–on–mirror nanogaps. *Phys. Rev. A – At. Mol. Opt. Phys.* **92**, 053811 (2015).
20. Mertens, J. *et al.* Tracking Optical Welding through Groove Modes in Plasmonic Nanocavities. *Nano Lett.* **16**, 5605–5611 (2016).
21. Jakubowicz, A., Jia, H., Wallace, R. M. & Gnade, B. E. Adsorption kinetics of p–nitrobenzenethiol self–assembled monolayers on a gold surface. *Langmuir* **21**, 950–955 (2005).
22. Canpean, V. & Astilean, S. Multifunctional plasmonic sensors on low–cost subwavelength metallic nanoholes arrays. *Lab Chip* **9**, 3574–3579 (2009).
23. Sheldon, M. T., Groep, J. van de, Brown, A. M., Polman, A. & Atwater, H. A. Plasmoelectric potentials in metal nanostructures. *Science (80–. ).* **346**, 828–831 (2014).
24. Novo, C., Funston, A. M., Gooding, A. K. & Mulvaney, P. Electrochemical Charging of Single Gold Nanorods. *J. Am. Chem. Soc.* **131**, 14664–14666 (2009).
25. Luo, Y. Large–scale preparation of single–crystalline gold nanoplates. *Mater. Lett.* **61**, 1346–1349 (2007).

26. Beeram, S. R. & Zamborini, F. P. Purification of Gold Nanoplates Grown Directly on Surfaces for Enhanced Localized Surface Plasmon Resonance Biosensing. *ACS Nano* **4**, 3633–3646 (2010).
27. Ha, T. H., Koo, H. & Chung, B. H. Shape Controlled Syntheses of Gold Nanoprism and Nanorod Influenced by Specific Adsorption of Halide Ions. *J. Phys. Chem. C* **111**, 1123–1130 (2007).
28. Millstone, J. E., Hurst, S. J., Métraux, G. S., Cutler, J. I. & Mirkin, C. A. Colloidal gold and silver triangular nanoprisms. *Small* **5**, 646–664 (2009).
29. Niu, Z. & Li, Y. Removal and utilization of capping agents in nanocatalysis. *Chem. Mater.* **26**, 72–83 (2014).
30. Li, D. *et al.* Surfactant removal for colloidal nanoparticles from solution synthesis: The effect on catalytic performance. *ACS Catal.* **2**, 1358–1362 (2012).
31. Ansar, S. M. *et al.* Removal of molecular adsorbates on gold nanoparticles using sodium borohydride in water. *Nano Lett.* **13**, 1226–1229 (2013).
32. Luo, M. *et al.* Facile removal of polyvinylpyrrolidone (PVP) adsorbates from Pt alloy nanoparticles. *J. Mater. Chem. A* **3**, 2770–2775 (2015).

## Abstract (in Korean)

금속 나노 입자에 빛이 쏘여질 경우 금속 나노 입자의 표면 전자가 국소적으로 진동하는 국소표면플라스몬 (LSP)이 발생하게 된다. 국소표면플라스몬은 나노 입자의 성질을 결정하는 중요한 요소이며, 따라서 나노 입자의 응용을 위해 국소표면플라스몬에 관한 연구들이 많이 진행되고 있다. 보편적으로 국소표면플라스몬 연구는 양자 역학적 효과를 무시한 고전 역학적인 관점에서 진행이 되어왔는데 이는 실질적으로 일어나는 현상을 모두 설명할 수 없다. 최근 들어서는 양자 역학적인 현상인 터널 효과 등을 고려한 이론적 연구나 실험적 연구가 진행이 되고 있지만 아직까지는 연구가 미비한 상황이다.

본 연구에서는 터널 효과 정도가 다른 두 분자를 이용해 터널 현상이 국소표면플라스몬에 끼치는 영향을 연구하였다. 터널 효과를 연구하는 데에 있어 금속 나노 입자 구조에 따라 국소표면플라스몬 공명 파장이 불균일하게 나타나는 것이 문제가 되는데, 본 실험에서는 이를 극복하기 위해 4-nitrobenzenethiol (NBT) 분자의 광환원 반응을 통해 은 나노입자-NBT-금 박막 구조체에서 분자만 변화하였을 때의 국소표면플라스몬 공명 파장의 변화와 균일한 국소표면플라스몬 공명 파장을 가지는 나노 육면체-분자-단결정 금 박막 구조체에서 분자에 따른 국소표면플라스몬 공명 파장의 차이를 관찰하였다. 국소표면플라스몬 공명 스펙트럼의 경우 직접 구성한 공초점 암시야 현미경을 이용하여 측정하였으며, 이는 보편적으로 사용하는 암시야 현미경에 비해 더 효율적으로 스펙트럼을 관찰할 수 있다는 장점이 있다.

먼저 은 나노입자-NBT-금 박막 구조체에서 광환원 반응을 통해 NBT를 4-aminobenzenethiol (ABT)로 변화시켰을 때, 국소표면플라스몬 공명 파장이 단파장 영역으로 이동하는 현상이 관찰되었다. 이는 ABT 분자의 아민 작용기가 은 나노 입자와 공유

결합을 형성하여 터널 효과가 일어나는 정도가 증가하기 때문이다. 비록 더 정확한 결과를 얻기 위해서 추가적인 실험이 필요하지만, 이 결과를 통해 터널 현상이 국소표면플라스몬에 어떤 영향을 끼치는지 확인할 수 있었으며 나아가 분자를 통해 국소표면플라스몬 공명 파장을 조절할 수 있는 가능성을 확인할 수 있었다.

다음으로 균일한 국소표면플라스몬 공명 파장을 가지는 나노 육면체-분자-단결정 금 박막 구조체를 만들기 위해 단결정 금 박막을 합성하였다. 선행 연구에서 보고된 방법을 변주하여 한 변이 5  $\mu\text{m}$  이상이고 두께가 약 30 nm 정도인 단결정 금 박막을 형성하였으며, 용매로 세척하여 표면 활성 물질을 제거하였다. 이렇게 형성된 나노 육면체-분자-단결정 금 박막 구조체에서 분자를 변화시켜 국소표면플라스몬에 터널 효과가 끼치는 영향을 연구할 예정이다.